



A 2-D model for friction of complex anisotropic surfaces

Gianluca Costagliola^a, Federico Bosia^a, Nicola M. Pugno^{b,c,d,*}

^a Department of Physics and Nanostructured Interfaces and Surfaces Centre, University of Torino, Via Pietro Giuria 1, Torino, 10125, Italy

^b Laboratory of Bio-Inspired & Graphene Nanomechanics, Department of Civil, Environmental and Mechanical Engineering, University of Trento, Via Mesiano, 77, Trento 38123, Italy

^c School of Engineering and Materials Science, Queen Mary University of London, Mile End Road, London E1 4NS, UK

^d Ket Labs, Edoardo Amaldi Foundation, Italian Space Agency, Via del Politecnico snc, Rome 00133, Italy

ARTICLE INFO

Article history:

Received 24 July 2017

Revised 7 November 2017

Accepted 16 November 2017

Available online 20 November 2017

Keywords:

Friction

Numerical models

Microstructures

Anisotropic materials

ABSTRACT

The friction force observed at macroscale is the result of interactions at various lower length scales that are difficult to model in a combined manner. For this reason, simplified approaches are required, depending on the specific aspect to be investigated. In particular, the dimensionality of the system is often reduced, especially in models designed to provide a qualitative description of frictional properties of elastic materials, e.g. the spring-block model. In this paper, we implement for the first time a two dimensional extension of the spring-block model, applying it to structured surfaces and investigating by means of numerical simulations the frictional behaviour of a surface in the presence of features like cavities, pillars or complex anisotropic structures. We show how friction can be effectively tuned by appropriate design of such surface features.

© 2017 Elsevier Ltd. All rights reserved.

1. Introduction

The frictional behavior of macroscopic bodies arises from various types of interactions occurring at different length scales between contact surfaces in relative motion. While it is clear that their ultimate origin lies in inter-atomic forces, it is difficult to scale these up to the macroscopic level and to include other aspects such as dependence on surface roughness, elasticity or plasticity, wear and specific surface structures (Nosonovsky and Bhushan, 2007; Persson, 2000). Moreover, the dependence on “external parameters”, e.g. relative sliding velocity of the surfaces and normal pressure, is neglected in approximate models such as the fundamental Amontons–Coulomb law, and violations of the latter have been observed (Deng et al., 2012; Katano et al., 2014).

For these reasons, simplified models are required in theoretical studies and numerical simulations, and friction problems can be addressed in different ways depending on the specific aspects under consideration. In order to improve theoretical knowledge of friction, or to design practical applications, it is not necessary to simulate all phenomena simultaneously, and a reductionist approach can be useful to investigate individual issues. Thus, despite the improvement in computational tools, in most cases it is still preferable to develop simplified models to describe specific aspects, aiming to provide qualitative understanding of the fundamental physical mechanisms involved.

One of the most used approaches to deal with friction of elastic bodies consists in the discretization of a material in springs and masses, as done e.g. in the Frenkel–Kontorova model (Braun and Kivshar, 2004), or the Burridge–Knopoff model

* Corresponding author.

E-mail addresses: gcostagl@unito.it (G. Costagliola), fbosia@unito.it (F. Bosia), nicola.pugno@unitn.it (N.M. Pugno).

(Burrige and Knopoff, 1967), the latter also known as the spring-block model. For simplicity, these models are often formulated in one dimension along the sliding direction, in various versions depending on the specific application. In recent years, interesting results have been obtained with these models, explaining experimental observations (Amundsen et al., 2012; Bouchbinder et al., 2011; Maegawa et al., 2010; Rubinstein et al., 2004; Scheibert and Dysthe, 2010; Trømborg et al., 2011). The extension to two dimensions is the straightforward improvement to better describe experimental results and to correctly reproduce phenomena occurring in two dimensions. This has already been done for some systems, like the Frenkel–Kontorova model (Mandelli et al., 2015; Norell et al., 2016) and the spring-block model applied to geology (Andersen, 1994; Brown et al., 1991; Giacco et al., 2014; Mori and Kawamura, 2008a; Mori and Kawamura, 2008b; Olami et al., 1992), but much work remains to be done to describe the friction of complex and structured surfaces.

The interest of this study lies not only in the numerical modeling of friction in itself, but also in the practical aspects that can be addressed: there are many studies relative to bio-inspired materials (Baum et al., 2014; Li et al., 2016; Murarash et al., 2011; Yurdumakan et al., 2005) or biological materials (Autumn et al., 2000; Labonte et al., 2014; Stempfle and Brendle, 2006; Stempfle et al., 2009; Varenberg et al., 2010) that involve non-trivial geometries that cannot be reduced to one-dimensional structures in order to be correctly modeled.

The one dimensional spring-block model was originally introduced to study earthquakes (Carlson and Langer, 1989; Carlson et al., 1994; Xia et al., 2005) and has also been used to investigate many aspects of dry friction of elastic materials (Amundsen et al., 2015; Braun et al., 2009; Capozza and Pugno, 2015; Capozza et al., 2011; Capozza and Urbakh, 2012; Pugno et al., 2013; Trømborg et al., 2015). In Costagliola et al. (2016), we have extensively investigated the general behavior of the model and the effects of local patterning (regular and hierarchical) on the macroscopic friction coefficients, and in Costagliola et al. (2017a) we have extended the study to composite surfaces, i.e. surfaces with varying material stiffness and roughness; finally in Costagliola et al. (2017b) we have introduced the multiscale extension of the model to study the statistical effects of surface roughness across length scales.

In this paper, we propose a 2-D extension of the spring-block model to describe the frictional behavior of an elastic material sliding on a rigid substrate. Our main aim is to compare the results with those obtained in the one-dimensional case and to extend the study to more complex surface structures, e.g. isotropic or anisotropic arrangements of cavities or pillars, simulating those found in biological materials. The two-dimensional spring-block model allows to consider a more realistic cases and captures a variety of behaviors that can be interesting for practical applications.

The paper is organized as follows: in Section 2, we present the model; in Section 3.1, we discuss the main differences with the one-dimensional case and we explore the role of the parameters without surface structures, highlighting the phenomenology of the model; in Section 3.2, we present the results for standard 1-D and 2-D surface structures like grooves and cavities; in Sections 3.3 and 3.4, we consider more complex cases of anisotropic surface patterning; finally, in Section 4, conclusions and future developments are discussed.

2. Model

The equation of motion for an isotropic linear elastic body driven by a slider on an infinitely rigid plane with damping and friction can be written as: $\rho \ddot{u} = \mu \nabla^2 u + (\lambda + \mu) \nabla (\nabla \cdot u) - \gamma \rho \dot{u}$, where u is the displacement vector, ρ is the mass density, γ is the damping frequency, λ , μ are the Lamé constants. The following boundary conditions must be imposed: the top surface of the body is driven at constant velocity v , the bottom surface is subjected to a spatially variable local friction force, which we discuss below, representing the surface interactions between the elastic body and the rigid plane, while free boundary conditions are set on the remaining sides.

In order to simulate this system, we extend the spring-block model to the two-dimensional case: the contact surface is discretized into elements of mass m , each connected by springs to the eight first neighbors and arranged in a regular square mesh (Fig. 1) with N_x contact points along the x -axis and N_y contact points along the y -axis. Hence, the total number of blocks is $N_b \equiv N_x N_y$. The distances on the axis between the blocks are, respectively, l_x and l_y . The mesh adopted in previous studies of the 2-D spring-block model, e.g. Olami et al. (1992) and Giacco et al. (2014), does not include diagonal springs, but we add them to account for the Poisson effect (our mesh is similar to that used in Trømborg et al. (2011)).

In order to obtain the equivalence of this spring-mass system with a homogeneous elastic material of Young's modulus E , the Poisson's ratio must be fixed to $\nu = 1/3$ (Absi and Prager, 1975), which corresponds to the plane stress case, $l_x = l_y \equiv l$ and $K_{int} = 3/8El_z$, where l_z is the thickness of the 2-D layer and K_{int} is the stiffness of the springs connecting the four nearest neighbors of each block, i.e. those aligned with the axis. The stiffness of the diagonal springs must be $K_{int}/2$. Hence, the internal elastic force on the block i exerted by the neighbor j is $\mathbf{F}_{int}^{(ij)} = k_{ij}(r_{ij} - l_{ij})(\mathbf{r}_j - \mathbf{r}_i)/r_{ij}$, where \mathbf{r}_i , \mathbf{r}_j are the position vectors of the two blocks, r_{ij} is the modulus of their distance, l_{ij} is the modulus of their rest distance and k_{ij} is the stiffness of the spring connecting them.

All the blocks are connected, through springs of stiffness K_s , to the slider that is moving at constant velocity v in the x direction, i.e. the slider vector velocity is $\mathbf{v} = (v, 0)$. Given the initial rest position \mathbf{r}_i^0 of block i , the shear force is $\mathbf{F}_s^{(i)} = K_s(\mathbf{v}t + \mathbf{r}_i^0 - \mathbf{r}_i)$. We define the total driving force on i as $\mathbf{F}_{mot}^{(i)} = \sum_j \mathbf{F}_{int}^{(ij)} + \mathbf{F}_s^{(i)}$. The stiffness K_s can be related to the macroscopic shear modulus $G = 3/8E$, since all the shear springs are attached in parallel, so that by simple calculations we obtain $K_s = K_{int}l^2/l_z^2$. In the following, for simplicity we fix $l_z = l$. This formulation, commonly used in spring-block models, neglects the long-range interactions that may arise from wave propagation through the bulk (Elbanna 2011; Hulikal et al.,

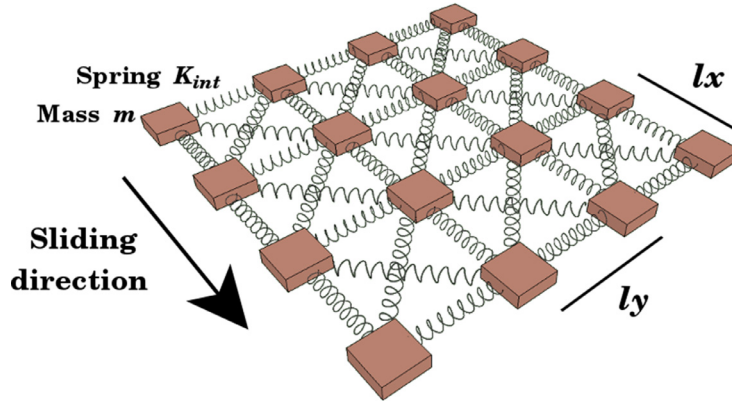


Fig. 1. Discretization of a square surface into a 2-D spring-block model, showing the mesh of the internal springs. The shear springs K_s modeling the block interaction with the slider are not shown.

2015; Rice, 1993; Rice and Ruina, 1983). Here, we suppose that the local interactions are dominating, which is a reasonable assumption for slow sliding velocities typical of the experiments we use as benchmarks (Baum et al., 2014; Li et al., 2016; Murarash et al., 2011). This assumption has already allowed to obtain correct descriptions of the phenomena occurring at the transition from static to dynamic friction (Braun et al., 2009; Trømborg et al., 2015).

The interactions between the blocks and the rigid plane can be introduced in many ways: in the original paper on the spring block model (Burrige and Knopoff, 1967) and in earthquake related papers, e.g. Olami et al. (1992) and Mori and Kawamura (2008a), it is introduced by means of an effective velocity-dependent force (Dieterich, 1979; Rice et al., 2001), in friction studies, e.g. Amundsen et al. (2012) and Braun et al. (2009), by springs that attach and detach during motion, in Trømborg et al. (2011) and Giacco et al. (2014) by means of the classical Amontons–Coulomb (AC) friction force. These various approaches give rise to slightly different quantitative results, but if they are implemented under reasonable assumptions, they do not significantly affect the overall predictions of the model, which is thought to provide a qualitative understanding of the basic mechanisms of friction. This is true at least for the small sliding velocities we are considering compared to the characteristic velocity scales of the system, i.e. $l\sqrt{K_{int}/m}$. A different qualitative behavior may arise for higher sliding velocities, as shown for rate-and-state friction laws (Elbanna and Heaton, 2012; Heaton, 1990; Zheng and Rice, 1998). In these cases, a careful evaluation of the interplay between the friction law and sliding velocity of the system must be performed.

In this study, we adopt a spring-block model based on the AC friction force and a statistical distribution on the friction coefficients (Costagliola et al., 2016; 2017a; 2017b): while the block i is at rest, the friction force $\mathbf{F}_{fr}^{(i)}$ is opposed to the total driving force, i.e. $\mathbf{F}_{fr}^{(i)} = -\mathbf{F}_{mot}^{(i)}$, up to a threshold value $F_{fr}^{(i)} = \mu_{si} F_n^{(i)}$, where μ_{si} is the static friction coefficient and $F_n^{(i)}$ is the normal force acting on i . When this limit is exceeded, a constant dynamic friction force opposes the motion, i.e. $\mathbf{F}_{fr}^{(i)} = -\mu_{di} F_n^{(i)} \hat{\mathbf{r}}_i$, where μ_{di} is the dynamic friction coefficient and $\hat{\mathbf{r}}_i$ is the velocity direction of the block. In the following, we will drop the subscripts s, d every time the considerations apply to both the coefficients.

The friction coefficients are extracted from a Gaussian statistical distribution to account for the randomness of the surface asperities, i.e. $p(\mu_i) = (\sqrt{2\pi}\sigma)^{-1} \exp[-(\mu_i - (\mu)_m)^2 / (2\sigma^2)]$, where $(\mu)_m$ denotes the mean of the microscopic friction coefficients and σ is its standard deviation. In order to simulate the presence of patterning or of structures on the surface, we set to zero the friction coefficients of the blocks located on zones detached from the rigid plane. The microscopic static and dynamic friction coefficients are fixed conventionally to $(\mu_s)_m = 1.0(1)$ and $(\mu_d)_m = 0.50(5)$, respectively, where the numbers in brackets denote the standard deviations of their Gaussian distributions.

The macroscopic friction coefficients are denoted with $(\mu)_M$. The static friction coefficient is calculated from the first maximum of the total friction force, while the dynamic one as the time average over the kinetic phase. To calculate the friction coefficients as ratio between longitudinal force and normal force, the norm of the longitudinal force vector must be calculated. When calculating time averages, care must be taken in the order of the operations: if there is an inversion of the friction force (i.e. some blocks exceed the rest position, as in the analytical calculations of Costagliola et al. (2016)) or a periodic motion takes place, switching the operations of norm and time average produces different results. In these cases, the calculation closer to the realistic experimental procedure must be adopted. However, in the results below, we have checked that the above conditions do not occur and the order of the operations is irrelevant. The model does not include roughness variations during sliding or other long term effects, so that the results for dynamic friction are to be considered within the limits of this approximation.

A damping force is added to eliminate artificial block oscillations: in Braun et al. (2009) and in the papers based on it (e.g. Capozza and Pugno, 2015) this is done by means of a viscous damping force proportional to the velocity of the block, i.e. $\mathbf{F}_d^{(i)} = -\gamma m \dot{\mathbf{r}}_i$. Another option, as in the 2-D model in Trømborg et al. (2011), is to impose the damping on the oscillations between each pair of blocks i and j , i.e. $\mathbf{F}_d^{(ij)} = -m\gamma (\dot{\mathbf{r}}_i - \dot{\mathbf{r}}_j)$, thus emulating the description usually adopted for viscoelastic

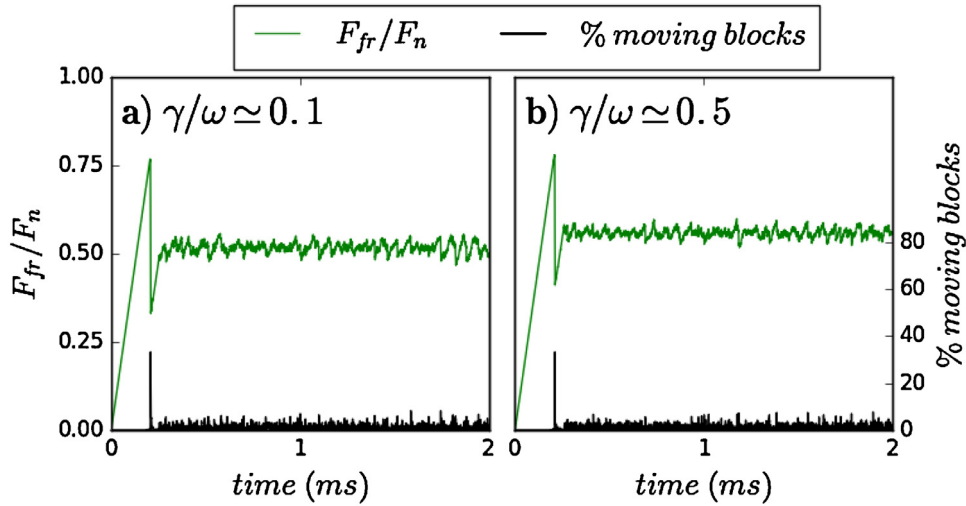


Fig. 2. Time evolution for the total friction force and percentage of moving blocks for $N = 20$, pressure $P = 0.1$ MPa, velocity $v = 0.1$ cm/s, $\gamma/\omega = 0.1$ (a) or $\gamma/\omega = 0.5$ (b), where ω is the internal frequency $\omega = \sqrt{K_{int}/m}$. The other parameters are set to the default values. Greater damping enhances the dynamic friction coefficient and reduces stick-slip oscillations.

materials (Banks et al., 2011; Carbone and Putignano, 2013; Hunter, 1961; Krushynska et al., 2016; Persson, 2001; Tschöegl 1989). In Section 3.1, we discuss the different behavior obtained with the two approaches, but in the following we adopt the former one, which is the simplest to allow damping of non-physical oscillations.

Thus, the complete equation of motion for block i is: $m\ddot{\mathbf{r}}_i = \sum_j \mathbf{F}_{int}^{(ij)} + \mathbf{F}_s^{(i)} + \mathbf{F}_{fr}^{(i)} + \mathbf{F}_d^{(i)}$. The overall system of differential equations is solved using a fourth-order Runge–Kutta algorithm. In order to calculate the average of any observable, the simulation must be iterated, extracting each time new random friction coefficients. In repeated tests, an integration time step $h = 10^{-8}$ s proves to be sufficient to reduce integration errors under the statistical uncertainty in the range adopted for the parameters of the system.

We consider only a square mesh, i.e. $N_x = N_y = N$, and we will specify the number of blocks for each considered case. The default normal pressure is $P = 0.05$ MPa, so that the normal force on each block is $F_n^{(i)} = Pl^2$ and the total normal force is $F_n = Pl^2N^2$. The slider velocity is $v = 0.05$ cm/s. We will discuss in Section 3.1 the motivations for these choices, but in any case the results display small dependence on these parameters.

Realistic macroscopic elastic properties are chosen, e.g. a Young's modulus $E = 10$ MPa, which is typical for a soft polymer or rubber-like material and a density $\rho = 1.2$ g/cm³. The distance between blocks l in the model is an arbitrary parameter representing the smallest surface feature that can be taken into account and is chosen by default as $l = 10^{-3}$ cm, so that the order of magnitude matches those typical of surface structures used in experiments (Baum et al., 2014; Li et al., 2016).

3. Results

3.1. Non-patterned surface

In this section, we model friction problems relative to homogeneous, non-patterned surfaces varying the fundamental parameters to understand the overall behavior and to compare it with that of the 1-D model studied in Costagliola et al. (2016). In Fig. 2, the friction force behavior as a function of time is shown with the default set of parameters: there is a linearly growing static phase up to the macroscopic rupture event, followed by a dynamic phase in which the system slides with small stick-slip oscillations at constant velocity v . The percentage of blocks in motion as a function of time is also shown: in the kinetic phase, single blocks or small groups slip simultaneously but not in a synchronized manner with respect to the rest of the surface.

The first difference with the 1-D model is that the 2D array of springs shown in Fig. 1 allows to correctly simulate the Poisson effect, i.e. a deformation in the transversal direction due to the stretching in the longitudinal one. Secondly, due to the model definition explained in Section 2, the stiffnesses do not depend on the total number of blocks, so that increasing N does not modify the elastic properties, but only the size of the system. Since the number of points grows as the square of the lateral size, $N \geq 100$ can already be considered a large system, as shown in Fig. 3, where the size effects on the global static friction coefficient are shown. Similar results hold for the dynamic friction. In the left (Fig. 3a) and right panels (Fig. 3b), the influence of the applied pressure P and the slider velocity v is also shown, respectively. In the typical ranges of

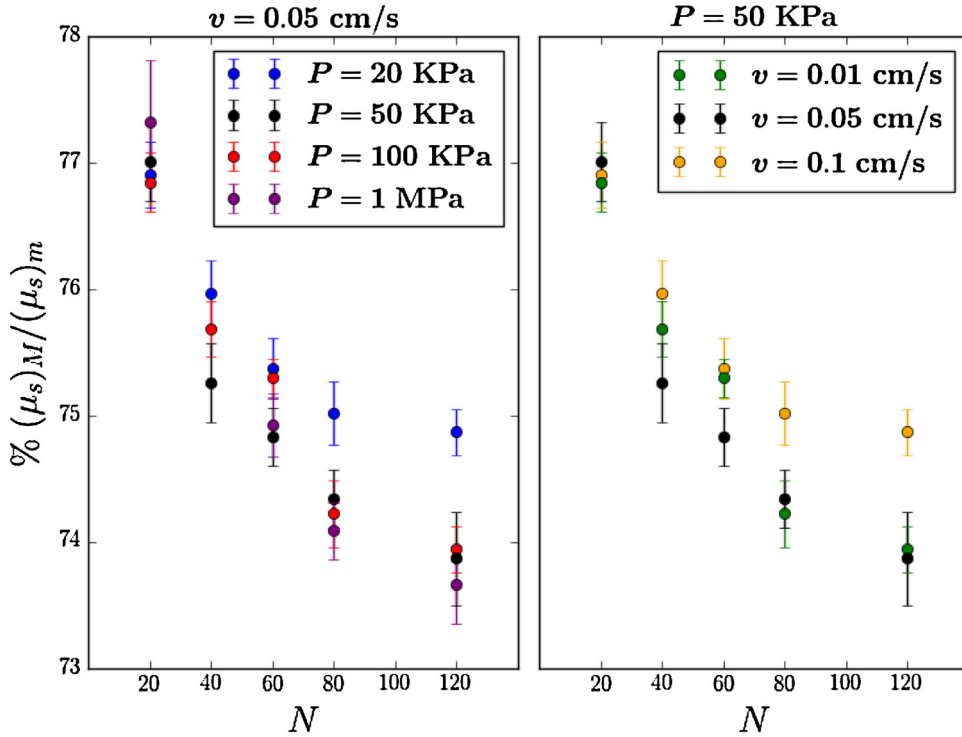


Fig. 3. Static friction coefficient as a function of the number of blocks N by varying the applied pressure P with the default velocity $v = 0.05 \text{ cm/s}$ (a), and by varying the velocity v with the default pressure $P = 50 \text{ KPa}$ (b). The black dots on both sides show the curve for the default set of parameters. Variations with respect to this are limited to a few percentage points in the typical ranges of these parameters.

these parameters, variations are limited within few percent, so that in the following we adopt typical values, e.g. $v = 0.05 \text{ cm/s}$ and $P = 50 \text{ KPa}$ without further discussions about their influence.

3.1.1. Role of damping

As mentioned, two possible approaches can be adopted to introduce viscous damping in the model. If we introduce a viscous damping force on the velocity, i.e. $\mathbf{F}_d^{(i)} = -\gamma m \dot{\mathbf{r}}_i$, there is an increase on the dynamic friction coefficient due to the damping which reduces the slip phases, similarly to the effect observed in Costagliola et al. (2016). This does not affect the general behavior of the system, as long as γ is in the underdamped regime, i.e. $\gamma < \omega \equiv \sqrt{K_{\text{int}}/m}$.

The other option consists in assuming the damping to be dependent on the relative velocity between blocks, i.e. $\mathbf{F}_d^{(ij)} = -m\gamma (\dot{\mathbf{r}}_i - \dot{\mathbf{r}}_j)$, thus reproducing the generalized Maxwell model for viscoelastic materials. This radically changes the previously-described kinetic phase: for small damping values, there is a limited increase of the dynamic friction with limited stick slip events, but for large damping, the fluctuations become larger and the kinetic phase consists in collective slips of the whole surface (Fig. 4). The explanation for this is that this type of damping favours the elimination of relative block oscillations, enhancing the coherence of the system, so that sliding events can involve a large number of blocks also during the kinetic phase. This behavior is highly non-trivial, since it is influenced not only by the sliding velocity or the elastic properties of the surface, but also by the discretization parameters, i.e. the number of blocks N : for example, with $N = 80$, the stick-slip oscillations are reduced, since for larger systems it is difficult to obtain collective slips and it is more likely that different portions of the surfaces move independently. Thus, the model can describe a variety of different situations and can capture the richness of behaviour of a structured viscoelastic material.

In the following, we adopt the first solution, i.e. a viscous damping force on the velocity of the blocks, since it provides a simpler approach for damping artificial block oscillations, and set $\gamma = 500 \text{ ms}^{-1}$ ($\gamma/\omega \approx 0.1$).

3.1.2. Detachment fronts

In this section, we focus on the transition from static to dynamic friction, corresponding to the maximum of the total friction force and its following drop, as shown in Fig. 2. The spring-block model has been used in many recent studies to obtain valuable insights on this aspect (Amundsen et al., 2012; Bouchbinder et al., 2011; Maegawa et al., 2010; Trømborg et al., 2011) and to confirm fundamental experimental observations about the onset of the dynamic motion (Ben-David et al., 2010; Rubinstein et al., 2004; 2007; Svetlizky and Fineberg, 2014). Our aim is not a detailed study of the wave propagation and the rupture fronts before the sliding phase, since many specific works have focused on these topics (Bayart et al., 2016;

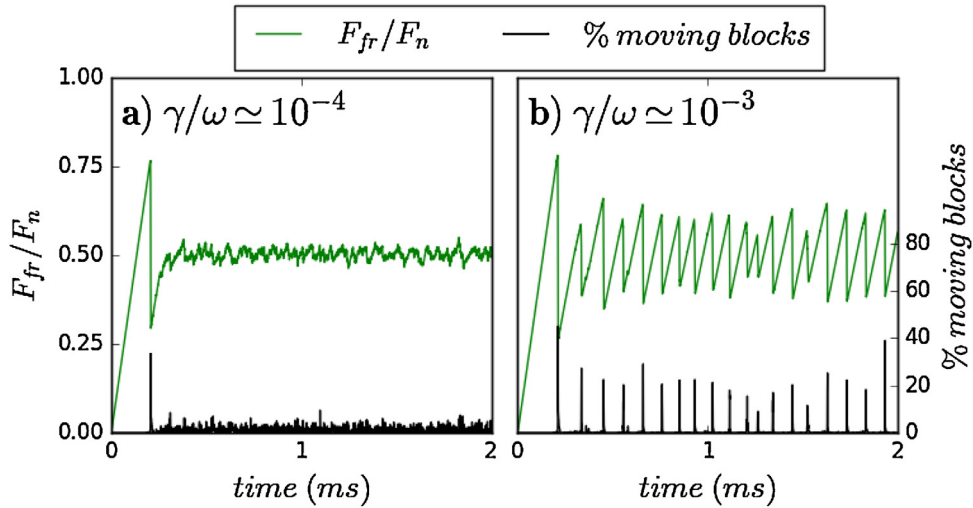


Fig. 4. Time evolution for the total friction force with the same parameters of Fig. 2, except that the damping is imposed on the relative velocity between neighboring blocks, i.e. using a viscoelastic material model, respectively with $\gamma/\omega = 10^{-3}$ (a) or $\gamma/\omega = 10^{-4}$ (b), where ω is the internal frequency ($\omega = \sqrt{K_{int}/m}$). The static friction coefficient remains unchanged, but the kinetic phase is markedly different, in particular for higher damping values when there are greater stick-slip oscillations.

Kammer et al., 2015; Lapusta and Rice 2003; Radiguet et al., 2013; Svetlizky et al., 2016; Urbakh et al., 2004), but to show how the 2-D model allows to qualitatively predict the phenomena illustrated in the literature.

In Fig. 5, four snapshots of the longitudinal deformation on the surface at different times of the transition are shown: starting from the points with the weakest static friction thresholds, rupture fronts propagate on the surface, until the whole surface slides (see the caption of Fig. 5 for a detailed description). The maximum force, i.e. the point in which the global static friction coefficient is calculated, occurs when the first rupture front begins its propagation; then the blocks are progressively reached by the rupture fronts and relax, and this corresponds to the phase with the drop of the friction force. This decrease ends when the whole surface has been reached by the rupture fronts and the overall sliding motion begins. At the beginning of the sliding, the spring mesh is frozen in a non-uniform distribution of regions of compression and tension. These regions tend to relax during the subsequent kinetic phase, in which different portions of the surface have continuous but incoherent stick-slip motion, and regions of residual stress remain. This has already been noted in 1-D models (Braun et al., 2009) and observed experimentally (Rubinstein et al., 2004), in terms of “memory effects” after the transition to kinetic friction (Amundsen et al., 2015). The surface deformation during the transition from static to dynamic friction is illustrated in Video1 together with the time evolution of the friction force.

In 2-D models, the shape of the rupture front in the horizontal plane can be studied: before the nucleation of a front, the detachment propagates first to the neighbors of the weakest threshold point along the sliding direction, so that the nucleation region is not a single point, but more likely a segment. For this reason, the fronts in Fig. 5 display an elliptical shape.

Many details of these simulations depend on the chosen parameters: the threshold distribution, which is a way to parametrize the surface roughness, but also the velocity and the elasticity of the material affect the number of fronts, the speed of propagation and the duration of the friction force decrease. Moreover, the model does not take into account the modification of the effective contact area during the transition. However, it is evident that the avalanches of ruptures originate from the regions with weakest thresholds and then propagate to the whole surface in all directions, similarly to avalanches in fracture mechanics (Bayart et al., 2016; Bouchbinder et al., 2011). Also, it is interesting to note the non-trivial persistence of residual deformations in correspondence with the regions of interaction between multiple detachment fronts, deriving from the inelastic nature of the model.

The role of the weakest thresholds is confirmed also in Costagliola et al. (2017a), where it is shown that the distribution of the static friction thresholds deeply affect the global static friction and the onset of motion, while it is almost irrelevant for the dynamic phase. Thus, in a real material the nucleation points could be the contact points with imperfect contact on the surface. On the basis of this observation, we discuss in the next sections how static friction can be radically modified by structures that give rise to non-trivial stress distributions on the surface before the sliding phase.

3.2. Patterned structures

First, we consider single-level surface structures, i.e. described by only one characteristic length scale, such as those shown in Fig. 6. The 2-D model allows to simulate more configurations than those studied in the 1-D case, e.g. in Costagliola et al. (2016), which is limited to structures similar to Fig. 6a. In experimental tests (Baum et al., 2014), grooves

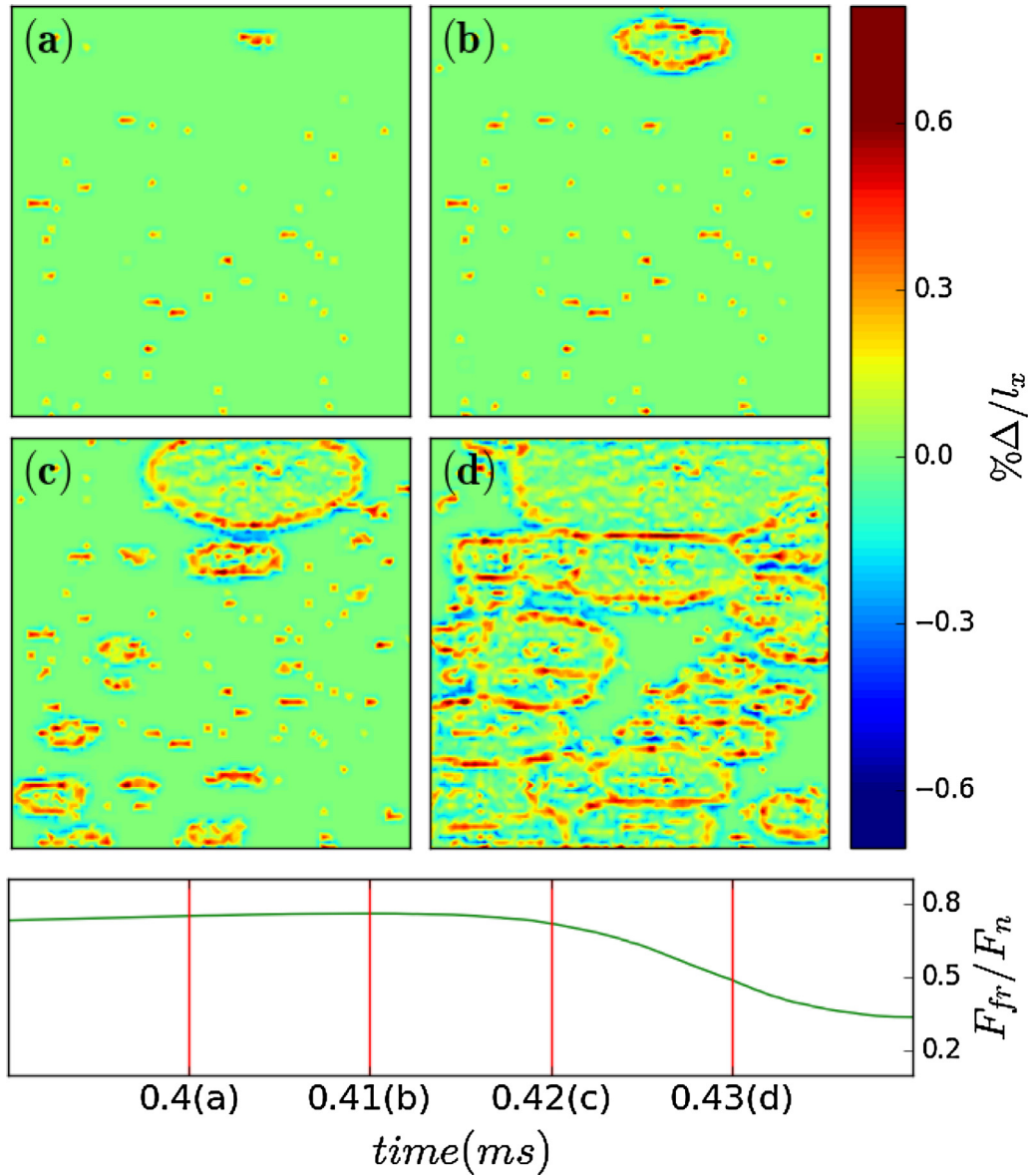


Fig. 5. Time snapshots of the spring mesh deformation $\Delta \equiv \sum_j F_{mt}^{(j)} / k_{ij}$ along the longitudinal direction on the surface normalized by the block distance l_x , so that positive values (red) indicate compression and negative values (blue) tension. Before the maximum of the friction force is reached, some blocks with weak static friction thresholds detach (a), then a rupture front nucleates from the weakest point, corresponding to the instant of the maximum force before the drop (b); the front propagates while other fronts nucleate elsewhere (c) finally, the whole surface slides leaving a non-uniform distribution of regions under tension/compression (d). (For interpretation of the references to colour in this figure legend, the reader is referred to the web version of this article.)

aligned with the sliding direction, like those in Fig. 6b, have also been considered, while square cavities and square pillars (Fig. 6c and d, respectively), are the simplest two dimensional structures that we can consider. Similar structures have been investigated experimentally (Greiner et al., 2014; He et al., 2008; Tay et al., 2011).

In order to simulate these structures, we set to zero the friction coefficients of the blocks corresponding to regions no longer in contact with the sliding plane. This is a 2-D model of the structures shown in Fig. 6, in which grooves correspond to regions without friction, while effects occurring in the depth direction are neglected, e.g. mechanical interlocking, geometric nonlinearities, and variability in stresses normal to the surface. However, this does not modify our general conclusions. To characterize the stress state of the surface, we define the surface stress field $\sigma \equiv \mathbf{F}_{mot} / l^2$, which in the static phase is equivalent to the tangential stress F_{fr} / l^2 for the regions in contact with the substrate. In the following, unless otherwise stated, we indicate as "stress" the modulus of σ , while we denote with σ_x and σ_y its components along the x- and y-axis, respectively.

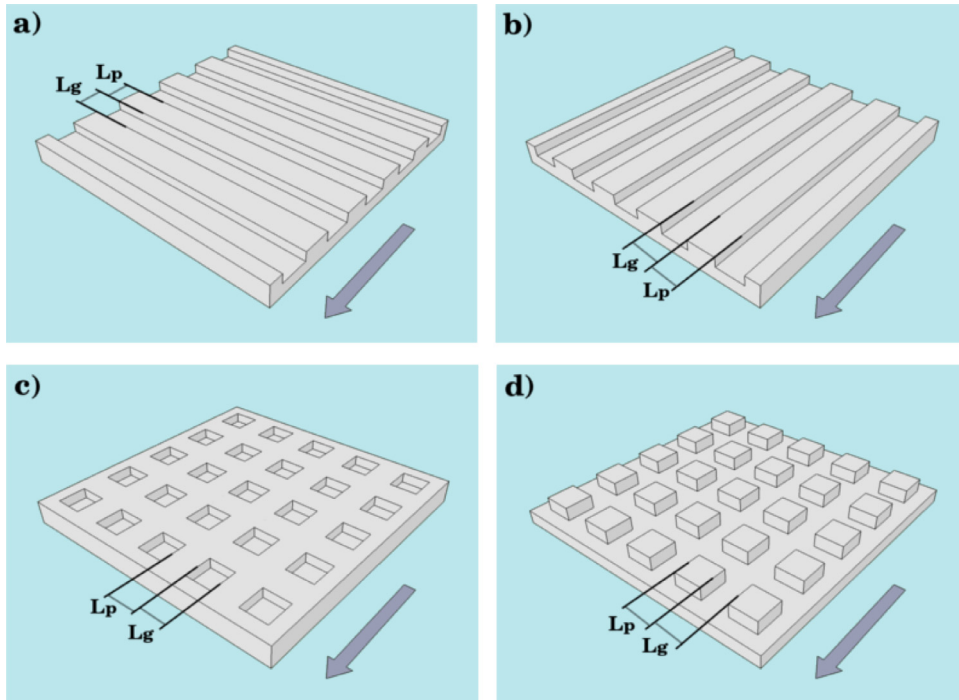


Fig. 6. Single-level surface structures considered in the simulations: patterning with grooves in direction perpendicular (a) or parallel (b) to the motion. Square cavities (c) and pillars (d). $n_g \equiv L_g/l_x$ is the ratio between the size of the structure and the elementary block distance. The arrow denotes the sliding direction. The patterns are modelled as 2-D surfaces but graphically represented as 3-D structures for illustrative purposes.

We denote with L_g the width of generic non contact regions, like grooves or holes, and with L_p the width of contact regions, like pillars or pawls, as shown in Fig. 6. The ratios $n_g \equiv L_g/l_x$ and $n_p \equiv L_p/l_x$ represent the number of blocks contained in these regions, which are convenient adimensional numbers to classify the width of the structure. In the following, if only n_g is reported, we are considering the case $n_g = n_p$. The system parameters are fixed to the default values with $N_x = N_y = 120$.

3.2.1. Static friction

In Costagliola et al. (2016) we have shown that in the static phase, i.e. before every block begins to slide, the surface stress is mostly concentrated at the edge of the grooves. Here, the same results are obtained and, more in general, we observe that stresses are concentrated at the edges of the structure in both directions, as shown in Fig. 7 for the structure with cavities. Due to the Poisson effect, stress components also appear in the transversal direction. For example, the structures in Fig. 6c tend to deform as a trapezoids with the longer side in the forward direction. Similar deformations occur in the case of grooves or other rectangular shapes. Vice versa, a square pillar structure, such as that in Fig. 6d, deforms like a trapezoid with the shorter side in the forward direction. Video 2 illustrates the time evolution of the total friction force and the longitudinal component of the surface stress distribution in the case of square cavities with $n_g=10$ (as in Fig. 7).

For a generic structure, the stresses are mostly concentrated where concave angles are present and where non-negligible stress components are present in both directions. From this we deduce that, other parameters being equal, a structure with a great number of concave angles and a large perimeter is expected to have considerably reduced static friction. Practical examples of such structures are presented in Section 3.3.

Results are shown in Fig. 8: in the case of surface patterning the well-known decrease in static friction is observed for larger grooves, but in this case the behaviour is not monotonic. The explanation for this is that, during the rupture process, the stress is redistributed on the surface in a non-trivial way: in the 1-D system, once the force thresholds of the edge blocks are exceeded, the stress is transferred only to the blocks adjacent to the edge, thus increasing the groove width but maintaining the patterned structure. In 2-D, instead, ruptures can be distributed in different locations along the transversal direction, so that the edge formed by attached blocks is no longer a regular pattern and could be, for example, a winding profile with a non-trivial surrounding stress distribution. This influences the transition from static to dynamic friction and, accordingly, the maximum of the total friction force. Videos 3 and 4 illustrate the time evolution of the total friction force and surface stress distribution (longitudinal component) in the case of transversal and longitudinal grooves, respectively, with $n_g=2$.

In other terms, the crack fronts are forced to propagate along the pawls. When they are narrow, i.e. for small n_g values, their dynamics is practically one-dimensional. If they are wider, the dynamics is determined by interactions of rupture

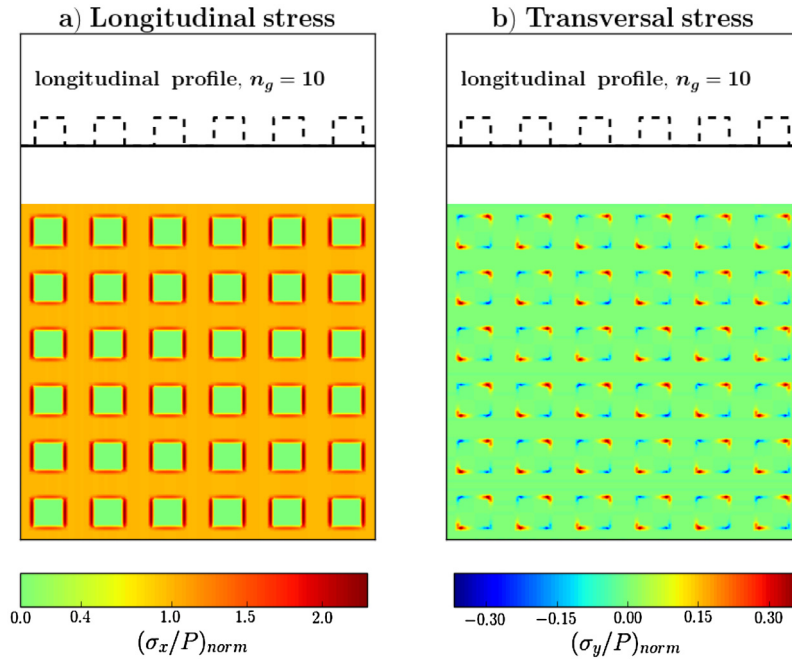


Fig. 7. Longitudinal (a) and transversal stress (b), normalized by the pressure on the 2-D surface, before the block motion, for a structure with square cavities as in Fig. 6c and $n_g = 10$ (the dotted lines above show the surface profile). The stress-pressure ratio is also normalized with the value obtained for a smooth surface, so that, for example, the normalized value is set to 1 for blocks away from the edges. The stress is accumulated at the edge of the cavities with a non-zero component in the transversal direction.

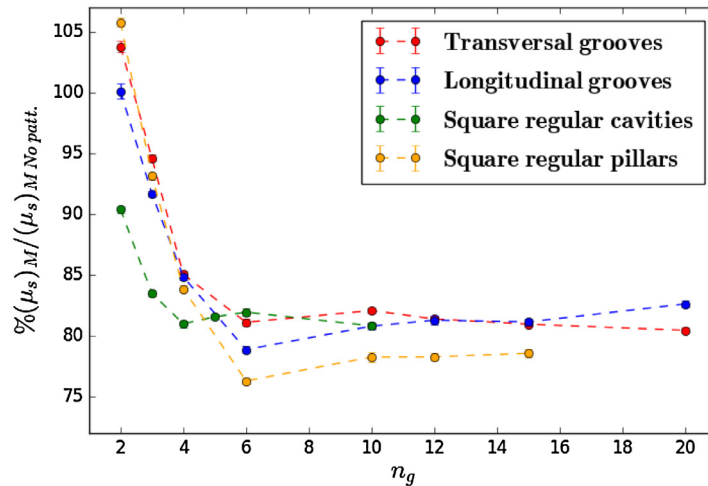


Fig. 8. Normalized static friction coefficients for the four single-level structures of Fig. 6. Results are normalized with respect to the static friction coefficients for a smooth surface (non-patterned case) and are displayed as a function of the structure characteristic width $n_g = n_p$. Notice the decrease of static friction for $n_g \approx 2$ and the non monotonic behavior for larger sizes ($n_g > 6$).

fronts in different directions, so that the overall behavior is more complicated and a non-monotonic dependence of static friction on n_g can arise. Moreover, before the sliding phase, the stress on the edges aligned with the sliding direction is slightly smaller than that on transversal ones, but the global static friction is larger for transversal grooves with respect to longitudinal ones (Fig. 8). This can be ascribed to the transition from static to dynamic friction: as noted in Section 3.1.2, the detachment front propagates first to the neighbors along the sliding direction, so that in the case of transversal grooves, the wave propagation is hampered due to the small pawl size, despite the stress being slightly larger. This is less influential for large n_g values and, indeed, the static friction is greater for longitudinal grooves. Overall, the interpretation of particular behaviors related to specific structures requires a detailed analysis of the onset of the dynamic motion for each specific case.

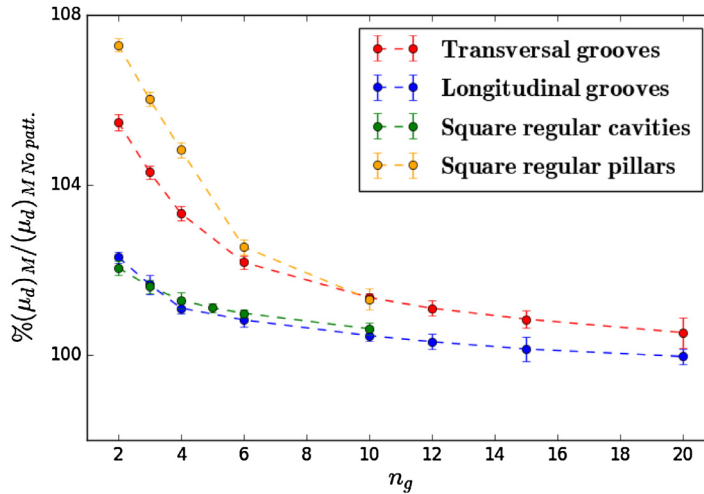


Fig. 9. Normalized dynamic friction coefficients for the four single-level structures of Fig. 6. Results are normalized with respect to the dynamic friction coefficients for a smooth surface (non-patterned case) and are displayed as a function of the structure typical width $n_g = n_p$. The decreasing trend with the size of the structures is limited to few percent with respect the non-patterned case.

The static friction coefficient for square cavities is the smallest of the considered structures for $n_g \leq 4$, but it does not decrease as significantly as for other structures for larger n_g values; a similar behaviour has been observed experimentally for bulk metal glass materials with honeycomb holes (Li et al., 2016), suggesting that the origin of the behaviour is related to the stress distribution determined by its structure rather than by the material.

Finally, the square pillars with regular spacing have the highest static friction for small n_g , but the smallest one for large n_g . The effective contact area for this structure is $S/S_{tot} = 1/4$, so that the static friction thresholds are doubled with respect the regular patterning. However, for larger pillars, the stress on the edges and concave angles (contrary to “hole” structures) increases and consistently with the argument above, the friction coefficient is reduced.

The static friction of such structures is qualitatively controlled by the width of the spacings (in our case n_g) and the effective contact area as in the 1-D case, but also by its shape and the orientation with respect to the sliding direction. In order to understand quantitatively which geometrical feature prevails, an accurate study of the stress distribution before the sliding and of the transition from static to dynamic friction is required, since in general simple proportionality laws cannot be formulated.

3.2.2. Dynamic friction

The dynamic friction coefficient in the presence of the considered structures displays small relative variations with respect to the non-patterned case. However, a trend can be observed, as reported in Fig. 9: the dynamic friction coefficients are always increased with respect the non-patterned case, and are reduced by increasing the size of the structures. This can be explained by considering that in this regime the dynamic motion entails the non-synchronized sliding of different parts of the surface, with an equilibrium between moving and stationary blocks. If the level of stress increases, there are more blocks moving and fewer subjected to static friction, so that the sum of the friction forces during sliding, which determines the total dynamic friction coefficient, decreases with n_g .

Comparing the four different structure types, the dynamic friction coefficients increase by reducing the effective contact area, as noted in Costagliola et al. (2016), but the geometry is also influential: the different behavior for longitudinal and transversal grooves, as explained for static friction, also influences the dynamic friction due to the blocks at rest during the dynamic phase.

3.3. Winding tread patterns

As observed in the previous section, with a general non-trivial surface structure, the stress concentrations before the sliding phase are localized at the edges and at the concave angles, so that for winding tread patterns we expect reduced static friction. This is confirmed by simulations on structures such as those shown in Fig. 10, in which the real contact area is the same of equal spaced grooves in Fig. 6a, b, but concave angles and perimeter are increased due to the winding profile of the grooves.

As observed in Costagliola et al. (2016), the effective contact area and the width of the spacings affect static friction too. Thus, in order to design a surface with a desired static friction coefficient, all of these three factors need to be considered. We consider for simplicity the case of Fig. 10 varying the size of the features: as in the previous section, L_g is the spacing between two consecutive structures along the sliding direction and L_p is the width of the structure. L_d is the width of

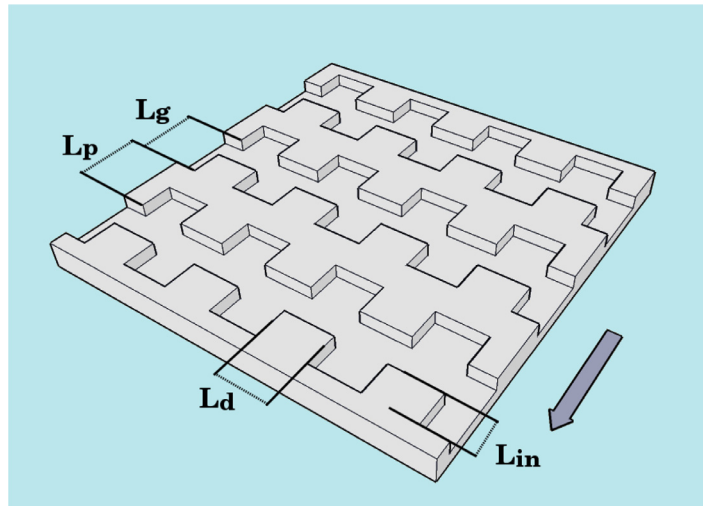


Fig. 10. Structure derived from that in Fig. 6a, in which the straight edge of the grooves has been modified to a winding profile with ratchets of width L_d and depth L_{in} . The effective contact area is halved, as in the case of regular patterning with grooves and pawls of the same size.

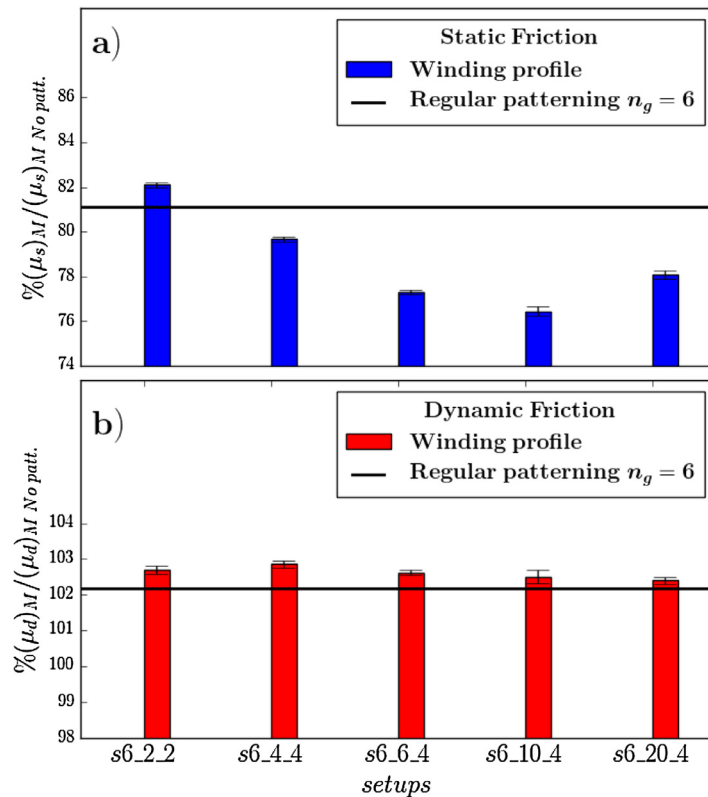


Fig. 11. Normalized static (a) and dynamic (b) friction coefficients for the different tread patterns in Table 1 compared to those for a regular patterning with $n_g = n_p = 6$ (black line). The static coefficient can be further reduced with respect to the case of periodic regular patterning.

the ratchets in the transversal direction to the sliding one and L_{in} is their indentation. By dividing these values by l_x , the values n_d and n_{in} are obtained, corresponding to the number of blocks for each feature in the width and length direction, respectively.

In Figs. 11 and 12 the friction coefficients of the various tread patterns are shown and, in the Table 1, their geometrical characteristics are reported. As expected from the previous discussion, static friction can be further reduced with respect to the case of periodic regular patterning with an increase of the perimeter and of the concave angles of the structures.

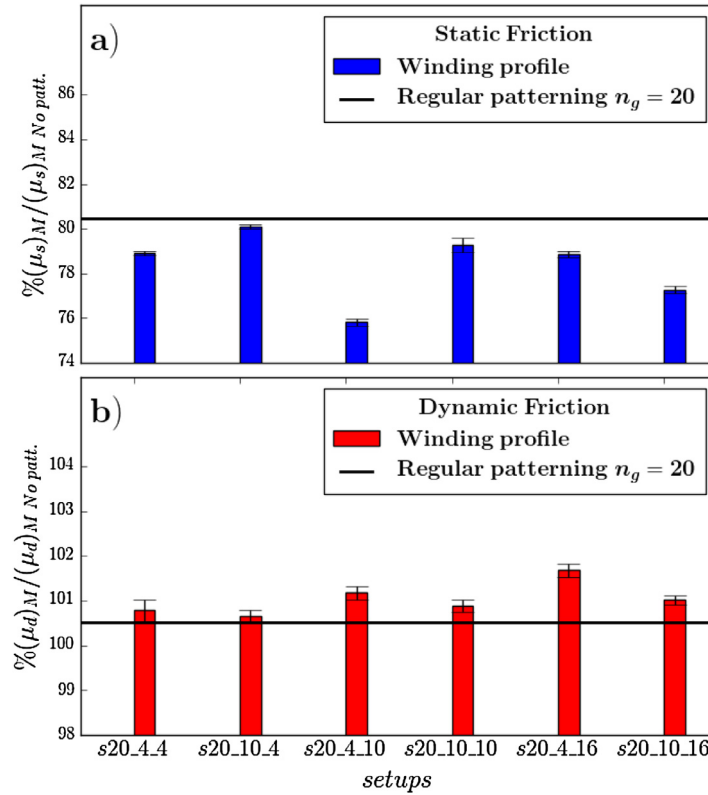


Fig. 12. Normalized static (a) and dynamic (b) friction coefficients for the different tread patterns in Table 1 compared to those for a regular patterning with $n_g = n_p = 20$ (black line). While the dynamic friction coefficient displays little variation, the static friction coefficient can be remarkably reduced with an optimal combinations of parameters.

Table 1

Table reporting the setups of the structure of Fig. 10 corresponding to the results presented in Figs. 11 and 12. For all the setups only n_g is reported since $n_p = n_g$.

Tread pattern	Grooves n_g	Width n_d	Depth n_{in}	Tread pattern	Grooves n_g	Width n_d	Depth n_{in}
s6_2_2	6	2	2	s20_4_4	20	4	4
s6_4_4	6	4	4	s20_10_4	20	10	4
s6_6_4	6	6	4	s20_4_10	20	4	10
s6_10_4	6	10	4	s20_10_10	20	10	10
s6_20_4	6	20	4	s20_4_16	20	4	16
				s20_10_16	20	10	16

Moreover, the precise value can be manipulated by varying the ratio between depth and width of structure, exploiting a high degree of tunability. There is an optimal configuration to obtain the maximum friction reduction, which involves ratchets whose depth is different than the width (e.g. configurations s6_10_4 and s20_4_10 in Table 1). The dynamic friction can also be manipulated, although the relative variations are smaller. Contrarily to the static friction case, these structures can enhance dynamic friction with respect to the corresponding regular structure.

Finally, by rotating the sliding direction perpendicularly to that shown in Fig. 10, similar qualitative considerations hold, though numerical results vary. For the configurations we have tested, only the s20_4_10 has the weakest static friction for both the direction. Thus, we can conclude that, by rotating these structures, results are not symmetric, but a configuration with small static friction coefficients in both directions can be found.

3.4. Anisotropic patterns

In Section 3.2, we discussed the different behavior obtained for longitudinal and transversal grooves, i.e. by rotating the grooves with respect to the sliding direction. In this section, we further investigate the role of anisotropic surface structures by considering, for example, rectangular pillars, as shown in Fig. 13.

By exploiting the mechanisms observed in Section 3.2, we find that with this structure static friction can vary significantly by rotating the sliding direction. Results are reported in Fig. 14, while in Table 2 the size of the sides are summarized.

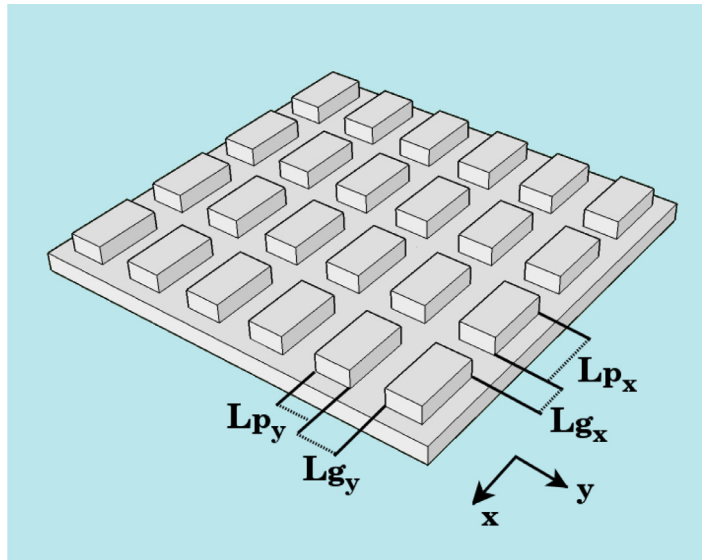


Fig. 13. Surface with rectangular pillars of size L_{px} , L_{py} and placed at L_{gx} , L_{gy} along the x and y direction, respectively. This simple configuration displays interesting properties due to anisotropy by switching the sliding direction between the x and y axis.

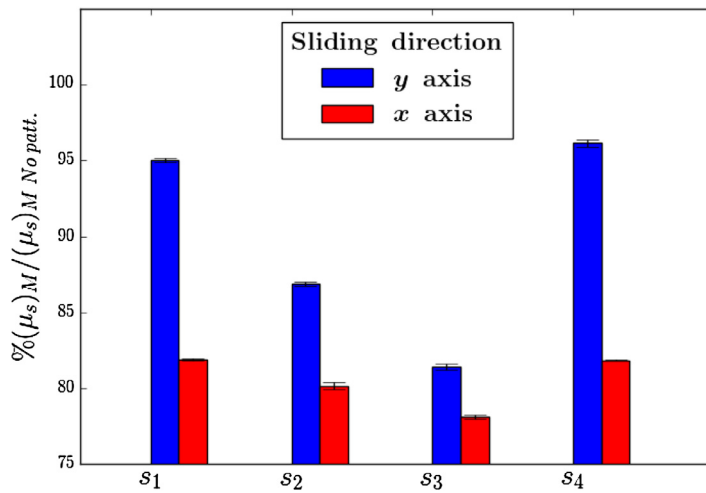


Fig. 14. Static friction coefficients for different sizes of anisotropic pillars in Table 2, normalized by the value for a smooth surface. The x and y axis are defined as in Fig. 13, i.e. the larger sides of the rectangular pillars are aligned with the x axis. There is a remarkable difference between the static friction coefficients in perpendicular sliding directions.

Table 2

Characteristics of the anisotropic pillars of Fig. 13 corresponding to the results presented in Fig. 14. We denote with n_{px} , n_{py} the sides of the pillars, and with n_{gx} , n_{gy} their distances along the x and y axis, respectively, expressed in number of elementary blocks.

data set	n_{px}	n_{py}	n_{gx}	n_{gy}
s_1	8	2	4	4
s_2	12	3	6	6
s_3	16	4	8	8
s_4	8	2	4	6

The pillar sides are denoted with L_{px} , L_{py} and their distances with L_{gx} , L_{gy} along the x and y axis, respectively. Dividing these by the length l , we obtain the ratios n_{px} , n_{py} , n_{gx} , n_{gy} , respectively. For rectangular pillars aligned with the sliding direction there is a remarkable reduction of static friction. Despite this result being intuitive, it is interesting to note the large difference in static friction that is exclusively due to the rotation of the sliding direction. The anisotropy of the structure and the underlying mechanisms occurring at the onset of sliding determine this behaviour. Thus, it appears that, to manipulate static friction with the sliding direction, anisotropic dimensions of the structure are more effective than complex shapes.

Additionally, we observe that, by increasing the size of the pillars, static friction decreases (as expected), and that the differences between the two directions are also reduced. This confirms that the effect is due to the mechanisms occurring during the transition from static to dynamic friction, as explained in Section 3.2.

4. Conclusions

In this paper, we have introduced a 2-D version of the spring-block model to investigate the friction coefficients of complex surfaces that cannot be reduced to one dimension. This model is fundamental for practical applications and to explain recent research results on friction of patterned surfaces in biological and bio-inspired materials. We have described the model in detail and presented benchmark results with a non-patterned surface, illustrating the effects of the model parameters, the general behavior of the system and to its consistency with results from the literature. We have also shown that interesting insights on friction can be obtained by investigating the transition from static to dynamic friction and the propagation of avalanche ruptures on the surface.

Next, we have considered simple patterned surfaces, e.g. longitudinal and transversal grooves, regular square cavities and pillars. Due to the Poisson effect, the in-plane surface stresses are non-zero in the transversal direction, so that structures like cavities deform and stretch in the forward sliding direction, while they undergo compression in the backward one, and vice versa for protruding structures like pillars. The surface stress is mostly concentrated at the edges and at concave angles. We have investigated how the friction coefficient is modified by varying the size of these structures, finding non-trivial behaviors that depend on the surface redistribution of stress during the transition from static to dynamic friction. The most interesting predictions are relative to the non-monotonic behavior of static friction by varying the size of the cavities (in agreement with experimental results) and the maximum static friction reduction obtained for structures with large regular square pillars.

Finally, we have considered winding tread patterns, which have the same contact area and the same spacings of regular groove patterns, but a greater number of concave angles and perimeter. As expected from the previous observations, we find a remarkable static friction reduction for some of these configurations. Thus, to manipulate the global static friction with structured surfaces, while in the 1-D case both the contact area and the width of the structures play a role, in the 2-D case the geometry of the edges also becomes fundamental. Fine tuning of static friction can also be achieved by varying the size of the specimens. Moreover, in the case of anisotropic structures like rectangular pillars, the friction coefficients can vary significantly with the sliding direction, which becomes an additional parameter to take into account. These kinds of predictions require a 2-D model such as the one presented herein that is able of capturing the non-trivial behavior of complex structures similar to those commonly observed in nature or employed in technological fields such as tire tread design.

Acknowledgments

N.M.P. is supported by the European Commission H2020 under the Graphene Flagship Core 1 No. 696656 (WP14 “Polymer Composites”) and FET Proactive “Neurofibres” grant No. 732344. G.C. and F.B. are supported by H2020 FET Proactive “Neurofibres” grant No. 732344. Computational resources were provided by the Centro di Competenza sul Calcolo Scientifico (C3S) of the University of Torino (c3s.unito.it) and by hpc@polito (<http://www.hpc.polito.it>).

Supporting Information

Supporting Information associated with this article can be found, in the online version, at [doi:10.1016/j.jmps.2017.11.015](https://doi.org/10.1016/j.jmps.2017.11.015).

References

- Absi, E., Prager, W., 1975. Comparison of equivalence and finite element methods. *Comp. Methods Appl. Mech. Eng.* 6, 59.
- Amundsen, D.S., Scheibert, J., Thøgersen, K., Trømborg, J., Malthé-Sørensen, A., 2012. 1D model of precursors to frictional stick-slip motion allowing for robust comparison with experiments. *Tribol. Lett.* 45, 357.
- Amundsen, D.S., Trømborg, J., Thøgersen, K., Katzav, E., Malthé-Sørensen, A., Scheibert, J., 2015. Steady-state propagation speed of rupture fronts along one-dimensional frictional interfaces. *Phys. Rev. E* 92, 032406.
- Andersen, V.J., 1994. Dynamical mean-field theory for a spring-block model of fracture. *Phys. Rev. B* 49, 9981.
- Autumn, K., Liang, Y., Hsieh, T., Zesch, W., Chan, W.-P., Kenny, T., Fearing, R., Full, R.J., 2000. Adhesive force of a single gecko foot-hair. *Nature* 405, 681.
- Banks, H.T., Hu, S., Kenz, Z.R., 2011. A brief review of elasticity and viscoelasticity for solids. *Adv. Appl. Math. Mech* 3, 1.
- Baum, M.J., Heepe, L., Fadeeva, E., Gorb, S.N., 2014. Dry friction of microstructured polymer surfaces inspired by snake skin. *Beilstein J. Nanotechnol.* 5, 1091.
- Bayart, E., Svetlizky, I., Fineberg, J., 2016. Fracture mechanics determine the lengths of interface ruptures that mediate frictional motion. *Nat. Phys.* 12, 166.
- Ben-David, O., Cohen, G., Fineberg, J., 2010. The dynamics of the onset of frictional slip. *Science* 330, 211.
- Bouchbinder, E., Brener, E.A., Barel, I., Urbakh, M., 2011. Slow cracklike dynamics at the onset of frictional sliding. *Phys. Rev. Lett.* 107, 235501.

- Braun, O.M., Barel, I., Urbakh, M., 2009. Dynamics of transition from static to kinetic friction. *Phys. Rev. Lett.* 103, 194301.
- Braun, O.M., Kivshar, Y.S., 2004. *The Frenkel-Kontorova Model: Concepts, Methods, and Applications*. Springer-Verlag, Berlin.
- Brown, S.R., Scholz, C.H., Rundle, J.B., 1991. A simplified spring-block model of earthquakes. *Geophys. Res. Lett.* 18, 215.
- Burridge, R., Knopoff, L., 1967. Model and theoretical seismicity. *Bull. Seismol. Soc. Am.* 57, 341.
- Capozza, R., Pugno, N.M., 2015. Effect of surface grooves on the static friction of an elastic slider. *Tribol. Lett.* 58, 35.
- Capozza, R., Rubinstein, S.M., Barel, I., Urbakh, M., Fineberg, J., 2011. Stabilizing stick-slip friction. *Phys. Rev. Lett.* 107, 024301.
- Capozza, R., Urbakh, M., 2012. Static friction and the dynamics of interfacial rupture. *Phys. Rev. B* 86, 085430.
- Carbone, G., Putignano, C., 2013. A novel methodology to predict sliding and rolling friction of viscoelastic materials: theory and experiments. *J. Mech. Phys. Solids* 61, 1822.
- Carlson, J.M., Langer, J.S., 1989. Properties of earthquakes generated by fault dynamics. *Phys. Rev. Lett.* 62, 2632.
- Carlson, J.M., Langer, J.S., Shaw, B.E., 1994. Dynamics of earthquake faults. *Rev. Mod. Phys.* 66, 657.
- Costagliola, G., Bosia, F., Pugno, N.M., 2016. Static and dynamic friction of hierarchical surfaces. *Phys. Rev. E* 94, 063003.
- Costagliola, G., Bosia, F., Pugno, N.M., 2017. Tuning friction with composite hierarchical surfaces. *Tribol. Int.* 115, 261.
- Costagliola, G., Bosia, F., Pugno, N.M., 2017. Hierarchical spring-block model for multiscale friction problems. *ACS Biomater. Sci. Eng.* 3, 11.
- Deng, Z., Smolyanitsky, A., Li, Q., Feng, X.Q., Cannara, R.J., 2012. Adhesion-dependent negative friction coefficient on chemically modified graphite at the nanoscale. *Nat. Mater.* 11, 1032.
- Dieterich, J.H., 1979. Modeling of rock friction: 1. experimental results and constitutive equations. *J. Geophys. Res.* 84, 2161.
- Elbanna, A.E., 2011. *Pulselike Ruptures on Strong Velocity-Weakening Frictional Interfaces: Dynamics and Implications*. Doctoral Dissertation. California Institute of Technology.
- Elbanna, A.E., Heaton, T.H., 2012. A new paradigm for simulating pulse-like ruptures: the pulse energy equation. *Geophys. J. Int.* 189, 1797.
- Giacco, F., Ciarrarra, M.P., Saggese, L., de Arcangelis, L., Lippiello, E., 2014. Non-monotonic dependence of the friction coefficient on heterogeneous stiffness. *Sci. Rep.* 4, 6772.
- Greiner, C., Schafer, M., Pop, U., Gumbsch, P., 2014. Contact splitting and the effect of dimple depth on static friction of textured surfaces. *Appl. Mater. Interfaces* 6, 7986.
- He, B., Chen, W., Wang, Q.J., 2008. Surface texture effect on friction of a microtextured poly(dimethylsiloxane) (PDMS). *Trib. Lett.* 31, 187.
- Heaton, T.H., 1990. Evidence for and implications of self-healing pulses of slip in earthquake rupture. *Phys. Earth Planet. In.* 64, 1.
- Hulikal, S., Bhattacharya, K., Lapusta, N., 2015. Collective behavior of viscoelastic asperities as a model for static and kinetic friction. *J. Mech. Phys. Solids* 76, 144.
- Hunter, S.C., 1961. The rolling contact of a rigid cylinder with a viscoelastic half space. *J. Appl. Mech.* 28, 611.
- Kammer, D.S., Radiguet, M., Ampuero, J.P., Molinari, J.F., 2015. Linear elastic fracture mechanics predicts the propagation distance of frictional slip. *Tribol. Lett.* 57, 23.
- Katano, Y., Nakano, K., Otsuki, M., Matsukawa, H., 2014. Novel friction law for the static friction force based on local precursor slipping. *Sci. Rep.* 4, 6324.
- Krushynska, A.O., Kouznetsova, V.G., Geers, M.G.D., 2016. Visco-elastic effects on wave dispersion in three-phase acoustic metamaterials. *J. Mech. Phys. Solids* 96, 29.
- Labonte, D., Williams, J.A., Federle, W., 2014. Surface contact and design of fibrillar 'friction pads' in stick insects (*carausius morosus*): mechanisms for large friction coefficients and negligible adhesion. *J. R. Soc. Interface* 11, 0034.
- Lapusta, N., Rice, J.R., 2003. Nucleation and early seismic propagation of small and large events in a crustal earthquake model. *J. Geophys. Res.* 108, 2205.
- Li, N., Xu, E., Liu, Z., Wang, X., Liu, L., 2016. Tuning apparent friction coefficient by controlled patterning bulk metallic glasses surfaces. *Sci. Rep.* 6, 39388.
- Maegawa, S., Suzuki, A., Nakano, K., 2010. Precursors of global slip in a longitudinal line contact under non-uniform normal loading. *Tribol. Lett.* 38, 3.
- Mandelli, D., Vanossi, A., Invernizzi, M., Ticco, S.V.P., Manini, N., Tosatti, E., 2015. Superlubric-pinned transition in sliding incommensurate colloidal monolayers. *Phys. Rev. B* 92, 134306.
- Mori, T., Kawamura, H., 2008. Simulation study of earthquakes based on the two-dimensional burridge-knopoff model with long-range interactions. *Phys. Rev. E* 77, 051123.
- Mori, T., Kawamura, H., 2008. Simulation study of the two-dimensional burridge-knopoff model of earthquakes. *J. Geophys. Res.* 113, B06301.
- Murarash, B., Itovich, Y., Varenberg, M., 2011. Tuning elastomer friction by hexagonal surface patterning. *Soft Matters* 7, 5553.
- Norell, J., Fasolino, A., de Wijn, A.S., 2016. Emergent friction in two-dimensional frenkel-kontorova models. *Phys. Rev. E* 94, 023001.
- Nosonovsky, M., Bhushan, B., 2007. Multiscale friction mechanisms and hierarchical surfaces in nano- and bio-tribology. *Mater. Sci. Eng. R* 58, 162.
- Olami, Z., Feder, H.J., Christensen, K., 1992. Self-organized criticality in a continuous, nonconservative cellular automaton modeling earthquakes. *Phys. Rev. Lett.* 68, 024301.
- Persson, B.N.J., 2000. *Sliding Friction - Physical principles and application*, in *Nanoscience and Technology*. Springer-Verlag, Berlin Heidelberg.
- Persson, B.N.J., 2001. Theory of rubber friction and contact mechanics. *J. Chem. Phys.* 115, 3840.
- Pugno, N.M., Yin, Q., Shi, X., Capozza, R., 2013. A generalization of the coulomb's friction law: from graphene to macroscale. *Meccanica* 48, 8.
- Radiguet, M., Kammer, D.S., Gillet, P., Molinari, J.F., 2013. Survival of heterogeneous stress distributions created by precursory slip at frictional interfaces. *Phys. Rev. Lett.* 111, 164302.
- Rice, J.R., 1993. Spatiotemporal complexity of slip on a fault. *J. Geophys. Res.* 98, 9885.
- Rice, J.R., Lapusta, N., Ranjith, K., 2001. Rate and state dependent friction and the stability of sliding between elastically deformable solids. *J. Mech. Phys. Solids* 49, 1865.
- Rice, J.R., Ruina, A.L., 1983. Stability of steady frictional slipping. *J. Appl. Mech.* 50, 343.
- Rubinstein, S.M., Cohen, G., Fineberg, J., 2004. Detachment fronts and the onset of dynamic friction. *Nature* 430, 1005.
- Rubinstein, S.M., Cohen, G., Fineberg, J., 2007. Dynamics of precursors to frictional sliding. *Phys. Rev. Lett.* 98, 226103.
- Scheibert, J., Dysthe, D.K., 2010. Role of friction-induced torque in stick-slip motion. *EPL* 92, 5.
- Stempfle, P., Brendle, M., 2006. Tribological behaviour of nacre-influence of the environment on the elementary wear processes. *Tribol. Int.* 39, 1485.
- Stempfle, P., Djilali, T., Njiwa, R.K., Rousseau, M., Lopez, E., Bourrat, X., 2009. Thermal-induced wear mechanisms of sheet nacre in dry friction. *Tribol. Lett.* 35, 97.
- Svetlizky, I., Fineberg, J., 2014. Classical shear cracks drive the onset of dry frictional motion. *Nature* 509, 205.
- Svetlizky, I., Munoz, D.P., Radiguet, M., Kammer, D.S., Molinari, J.F., Fineberg, J., 2016. Properties of the shear stress peak radiated ahead of rapidly accelerating rupture fronts that mediate frictional slip. *PNAS* 113, 542–547.
- Tay, N.B., Minn, M., Sinha, S.K., 2011. A tribological study of SU-8 micro-dot patterns printed on si surface in a flat-on-flat reciprocating sliding test. *Trib. Lett.* 44, 167.
- Trømborg, J., Scheibert, J., Amundsen, D.S., Thøgersen, K., Malthe-Sørensen, A., 2011. Transition from static to kinetic friction: insights from a 2d model. *Phys. Rev. Lett.* 107, 074301.
- Trømborg, J., Sveinsson, H.A., Thøgersen, K., Scheibert, J., Malthe-Sørensen, A., 2015. Speed of fast and slow rupture fronts along frictional interfaces. *Phys. Rev. E* 92, 012408.
- Tschoegl, N.W., 1989. *The Phenomenological Theory of Linear Viscoelastic Behavior*. Springer Verlag.
- Urbakh, M., Klafter, J., Gourdon, D., Israelachvili, J., 2004. The nonlinear nature of friction. *Nature* 430.
- Varenberg, M., Pugno, N.M., Gorb, S.N., 2010. Spatulate structures in biological fibrillar adhesion. *Soft Matter* 6, 3269.
- Xia, J., Gould, H., Klein, W., Rundle, J.B., 2005. Simulation of the burridge-knopoff model of earthquakes with variable range stress transfer. *Phys. Rev. Lett.* 95, 248501.

- Yurdumakan, B., Ravivkar, N.R., Ajayan, P.M., Dhinojwala, A., 2005. Synthetic gecko foot-hairs from multiwalled carbon nanotubes. *Chem. Commun.* 30, 3799.
- Zheng, G., Rice, J.R., 1998. Conditions under which velocity-weakening friction allows a self-healing versus a cracklike mode of rupture. *Bull. Seismol. Soc. Am.* 88, 1466.